



Effect of mesh wick geometry on the maximum heat transfer rate of flat-micro heat pipes with multi-heat sources and sinks



Bimal Subedi^a, Sung Hyoun Kim^a, Seok Pil Jang^{a,b,*}, M.A. Kedzierski^b

^a School of Aerospace and Mechanical Engineering, Korea Aerospace University, Goyang, Gyeonggi-do 412-791, Republic of Korea

^b National Institute of Standards and Technology, Bldg. 226, Rm B 114, Gaithersburg, MD 20899, USA

ARTICLE INFO

Article history:

Received 20 September 2018

Received in revised form 16 November 2018

Accepted 17 November 2018

Keywords:

Flat-micro heat pipes

Brinkman-extended Darcy equation

Maximum heat transfer rate

Optimized wick geometry

Capillary limit

Allowable maximum temperature limit

ABSTRACT

This paper presents a theoretical investigation of the thermal characteristics of flat-micro heat pipes (FMHPs) with multi-heat sources and sinks. Analytical solutions of the pressure and the temperature distributions of FMHPs with multi-heat sources and sinks were obtained based on the modified liquid pressure drop. The solutions were used to identify the key engineering parameters of a mesh wick with microscale length that affect the maximum heat transfer rate of the FMHPs with multi-heat sources and sinks. The effects of the key engineering parameters on the maximum heat transfer rate of the FMHPs were presented for two limits. The first limit is the capillary limit and the other is the allowable maximum temperature limit which is used to ensure that the maximum surface temperature of the FMHP with the maximum heat transfer rate calculated at the capillary limit does not exceed the allowable maximum temperature of the electronic components. Finally, the theoretical results for the optimized wick structure for the corresponding maximum heat transfer rate and the surface temperature distribution of the FMHP were compared for the capillary limit only and for the maximum temperature limit cases, respectively.

© 2018 Elsevier Ltd. All rights reserved.

1. Introduction

In recent years, continuous improvements in thermal management technology for electronic devices, such as tablet PCs, smartphones, and various kinds of mobile electronic devices, have been developed to meet the increasingly higher heat flux requirements due to their dramatic reduction in size [1–3].¹ One solution that has been devised by researchers [1,4–22] to meet the high heat flux duty is flat-micro heat pipes (hereafter FMHPs). FMHPs have a thickness of less than 1 mm; however, there are several challenges in developing devices at this scale. One of them is analyzing the thermal characteristics of the FMHPs with practical boundary conditions, which means multi-heat sources as shown in Fig. 1. Most researchers [1,9–12] present a simple model with a single heat source and sink to understand the thermal characteristics of FMHPs due to the simplicity. However, Lefevre and Lallemand [5], Rulliere et al. [6,9]

presented analytical models for the pressure and temperature distributions of FMHPs with multi-heat sources and sinks, and validated their models with experimental results, but their model [5,6] has two limitations. The first limitation is the Darcy model for predicting the liquid pressure distribution in the micro-length scale mesh wick is used because the model cannot consider the no-slip condition at the wall. As a result, the thermal resistance as well as maximum heat transfer rate of the FMHPs based on the model are not correctly modeled. The other limitation is they did not systematically present the effects of the key engineering parameters on the maximum heat transfer rate of the FMHPs with multi-heat sources and sinks.

The purpose of this paper is to present the analytical models for temperature and pressure distributions in a systematic way to clearly understand the thermal characteristics of FMHPs, which include a micro-length scale mesh wick with multi-heat sources and sinks. The mesh wick consists of a weaved bundle of fibers that act as pseudo capillary tubes with the liquid between the spaces of the fibers being the source of the “pumped” liquid. The most important contribution to the improvement in FMHP modeling is inclusion of the no-slip condition at the wall. This condition was included by analyzing the pressure distribution of liquid flow through the mesh wick as presented by Lefevre and Lallemand [5], and Rulliere et al. [6] but with the addition of a modified Brinkman-extended Darcy equation [23,24] that accounts for the

* Corresponding author at: School of Aerospace and Mechanical Engineering, Korea Aerospace University, Goyang, Gyeonggi-do 412-791, Republic of Korea.

E-mail address: spjang@kau.ac.kr (S.P. Jang).

¹ Certain trade names and company products are mentioned in the text or identified in an illustration in order to adequately specify the experimental procedure and equipment used. In no case does such an identification imply recommendation or endorsement by the National Institute of Standards and Technology, nor does it imply that the products are necessarily the best available for the purpose.

Nomenclature

a, b, c	FMHPs dimensions [m]
A_{m0}, A_{0m}, A_{mn}	Fourier coefficients of temperature
A	total area [m ²]
Bi	Biot number (hc/k_s)
B_{m0}, B_{0m}, B_{mn}	Fourier coefficients of heat flux
C_{m0}, C_{0m}, C_{mn}	Fourier coefficients of pressure
d	fiber diameter [m]
g	gravitational acceleration [m·s ⁻²]
G	dimensionless parameter
h_{fg}	latent heat of vaporization [J·kg ⁻¹]
h	equivalent heat transfer coefficient [W·m ⁻² K ⁻¹]
H	height [m]
k	thermal conductivity [W·m ⁻¹ K ⁻¹]
k_p	thermal conductivity of wick material [W·m ⁻¹ K ⁻¹]
K	permeability [m ²]
N	number of mesh layers
P	pressure [Pa]
Q	heat transfer rate [W]
r	pore radius [m]
T	temperature [K]
T_{sat}	saturation temperature [K]
T^*	dimensionless temperature relative to T_{sat}
\vec{U}_x	velocity along the x-axis [m·s ⁻¹]
\vec{U}_y	velocity along the y-axis [m·s ⁻¹]
w	fiber separation distance [m]
x, y, z	coordinates [m]
X, Y, Z	dimensionless coordinates

Greek symbols

β, ψ	dimensionless lengths
ε	porosity
η	ratio of the heat source area to the heat sink area
θ	contact angle
μ	dynamic viscosity [Pa·s]
ρ	density [kg·m ⁻³]
σ	surface tension [N·m ⁻¹]
$\phi(X, Y)$	non-dimension heat flux
φ	heat flux [W·m ⁻²]
φ_0	imposed heat flux [W·m ⁻²]

Subscripts

c	condenser, capillary
e	evaporator
eq	equivalent
eff	effective
l	liquid
s	solid
total	total
v	vapor
w	wick

Special symbol

$\langle \rangle$	averaged value by z-axis
-------------------	--------------------------

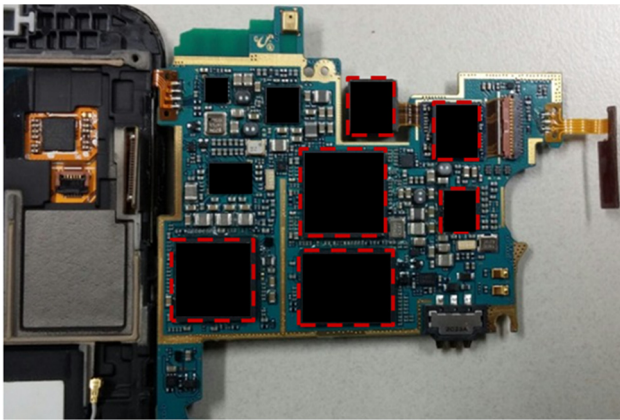


Fig. 1. Electronic components as multi-heat sources in commercial mobile electronic devices.

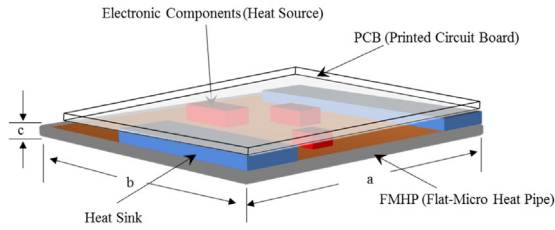
no-slip condition. The analytical models were used to identify the key engineering parameters of the mesh wick that affect the maximum heat transfer rate. The influence of the key parameters, such as fiber diameter, fiber separation distance, and wick thickness, on the maximum heat transfer rate were presented with two limits. One limit is the capillary limit which was widely used to determine the maximum heat transfer rate when capillary forces are no longer sufficient to deliver enough liquid flow for cooling. The other limit is the allowable maximum temperature limit [25] which can be defined by the allowable maximum temperature of the electronic components. This analysis ensures that the maximum surface temperature of the FMHP with the maximum heat transfer rate at the capillary limit does not exceed the

allowable maximum temperature of the electronic components. The optimized mesh wick for FMHPs with the maximum heat transfer rate was analytically presented using the two limits when the FMHPs had three heat sources and two heat sinks with distinct sizes. Finally, the theoretically results of the maximum heat transfer rate and the surface temperature distribution of the FMHP with the optimized wick are compared for the capillary and maximum temperature limits.

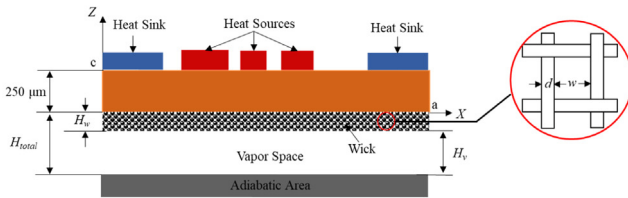
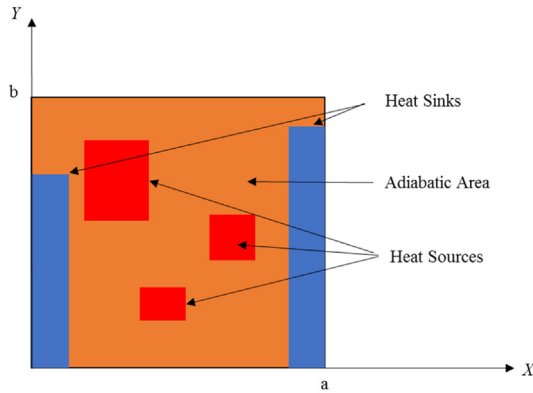
2. Analytical model

As shown in Fig. 1, PCBs (Printed Circuit Boards) for mobile electronic devices can contain many electronic components that act as high heat flux multi-heat sources. Fig. 2(a) shows how the FMHP can be used to simultaneously cool multi-heat sources on a PCB. Consequently, the problem under consideration as shown in Fig. 2(b) is to obtain the surface temperature distribution of the FMHP as well as the pressure distributions of the vapor and liquid inside the FMHP with three multi-heat sources and two heat sinks with distinct sizes. The surface temperature distribution of the FMHP was obtained from a three-dimensional heat conduction solution in the wall of the FMHP with multi-heat sources and sinks. The analytical solution of the surface temperature distribution was used to obtain the liquid and vapor pressure distributions in the FMHP.

Based on the results, the key engineering parameters of the mesh wick that affect the maximum heat transfer rate were identified. The Young-Laplace equation with the analytical solutions of liquid and vapor pressure distributions was used to determine the maximum heat transfer rate of the FMHP theoretically at the capillary limit. If the maximum temperature for this condition exceeded the allowable maximum temperature of the device components, then the calculated heat flux that corresponded to the



(a) Schematic view of a Flat-Micro Heat Pipe (FMHP)



(b) Geometry of a Flat-Micro Heat Pipe (FMHP)

Fig. 2. Schematic view of a Flat-Micro Heat Pipe (FMHP).

allowable temperature was set as the maximum heat transfer rate for the FMHP.

Fig. 2(b) shows the cross-sectional area of the FMHP which consists of a solid wall, a mesh wick modelled as a porous medium, and a vapor core. For the analysis, all properties were assumed to be constant and were evaluated at the saturated temperature of the working fluid. In addition, the gravitational force was assumed to be negligible.

2.1. Surface temperature distribution

The surface temperature distribution of the FMHP was obtained from a Fourier series solution of the 3D steady-state heat conduction equation presented by Feng and Xu [4], Lefevre and Lallemand [5], and Rulliere et al. [6].

3D steady state heat conduction equation

$$\frac{\partial^2 T^*}{\partial X^2} + \frac{1}{\beta^2} \frac{\partial^2 T^*}{\partial Y^2} + \frac{1}{\psi^2} \frac{\partial^2 T^*}{\partial Z^2} = 0 \quad (1)$$

Boundary conditions

$$\begin{aligned} \frac{\partial T^*}{\partial X} \Big|_{X=0} &= \frac{\partial T^*}{\partial X} \Big|_{X=1} = \frac{\partial T^*}{\partial Y} \Big|_{Y=0} = \frac{\partial T^*}{\partial Y} \Big|_{Y=1} = 0, \\ \frac{\partial T^*}{\partial Z} \Big|_{Z=0} &= Bi T^* = \frac{hc}{k_s} T^* \quad \text{where } h = \frac{k_{eq}}{H_w} \end{aligned} \quad (2)$$

$$k_{eq} = \frac{k_l [(k_l + k_p) - (1 - \varepsilon)(k_l - k_p)]}{(k_l + k_p) + (1 - \varepsilon)(k_l - k_p)} \quad (3)$$

$$\phi(X, Y) = \frac{\partial T^*}{\partial Z} \Big|_{Z=1} = \begin{cases} 1 & \text{in the heat source areas} \\ 0 & \text{in the adiabatic area} \\ -\eta & \text{in the heat sink areas} \end{cases} \quad \text{where } \eta = \frac{A_e}{A_c} \quad (4)$$

Included non-dimensional parameters

$$\begin{aligned} T^* &= \frac{k_s}{\varphi_o c} \Delta T, \quad \varphi_o = \frac{Q}{A_e}, \quad \beta = \frac{b}{a}, \quad \psi = \frac{c}{a}, \quad X = \frac{x}{a}, \\ Y &= \frac{y}{b}, \quad Z = \frac{z}{c} \quad \text{where } \Delta T = T - T_{sat} \end{aligned} \quad (5)$$

where T , T_{sat} , T^* are the local temperature, the saturation temperature, and the dimensionless temperature, respectively. The parameters a , b , c are the geometric dimensions of the FMHPs. In addition, the A_e , A_c , and Q are the total area of all heat sources, the total area of all heat sinks, and the heat transfer rate, respectively. The dimensional coordinates are x , y , and z . The non-dimensional coordinates are X , Y , and Z . The Biot number (Bi) is defined in Eq. (2). The ε , and the φ_o are the porosity of wick and the imposed heat flux, respectively. Finally, the k_l , k_p , k_s , and k_{eq} are the thermal conductivities of the working fluid, wick, wall and the equivalent thermal conductivity, respectively.

The non-dimensional heat flux (ϕ) can be expressed using the following expression [5]:

$$\begin{aligned} \phi(X, Y) &= \sum_{m=1}^{\infty} B_{m0} \cos(m\pi X) + \sum_{n=1}^{\infty} B_{0n} \cos(n\pi Y) + \sum_{n=1}^{\infty} \sum_{m=1}^{\infty} B_{mn} \\ &\times \cos(m\pi X) \cos(n\pi Y) \end{aligned} \quad (6)$$

The solution for the non-dimensional temperature (T^*) can be obtained from the steady-state heat conduction equation shown in Eq. (1) along with the boundary conditions given in Eqs. (2) and (4) as [4–6]:

$$\begin{aligned} T^* &= \sum_{m=1}^{\infty} A_{m0}(Z) \cos(m\pi X) + \sum_{n=1}^{\infty} A_{0n}(Z) \cos(n\pi Y) \\ &+ \sum_{n=1}^{\infty} \sum_{m=1}^{\infty} A_{mn}(Z) \cos(m\pi X) \cos(n\pi Y) \end{aligned} \quad (7)$$

where A_{m0} , A_{0n} , A_{mn} and B_{m0} , B_{0n} , B_{mn} are the Fourier coefficients, which are described in Lefevre and Lallemand [5], and Rulliere et al. [6].

2.2. Hydrodynamic models

The maximum heat transfer rate of FMHPs is dominantly governed by the liquid pressure distribution in the mesh wick because the liquid pressure drop through the mesh wick with micro-length scale is larger than the vapor pressure drop in the FMHPs. Consequently, a key purpose of this paper is to correct the simplification made by Lefevre and Lallemand [5], and Rulliere et al. [6] by analytically considering the no-slip condition at the FMHP's wall in the pressure distribution.

a. Liquid pressure distribution

The liquid pressure distribution through the micro-length scale mesh wick was obtained from the Brinkman-extended Darcy equation [23,24] (Eq. (8)) which considers the no-slip condition at the wall (the last boundary condition given in Eq. (9)):

Brinkman-extended Darcy Equation

$$\nabla P_{l,i} = -\frac{\mu}{K} \vec{U}_i + \mu \frac{\partial^2 \vec{U}_i}{\partial z^2} \quad \text{where } i = x, y \tag{8}$$

$$\text{B.C. } z = -\frac{H_w}{2} \quad \frac{\partial \vec{U}_i}{\partial z} = 0; \quad z = 0 \quad \vec{U}_i = 0 \tag{9}$$

Solving the differential equation given in Eq. (8) with its boundary conditions given in Eq. (9) leads to the analytical solutions of the x- and y-velocities in the wick liquid as:

$$\vec{U}_i = -\frac{\partial P_l}{\partial i} \frac{K}{\mu} \left\{ 1 - \frac{e\left(-\frac{z}{\sqrt{K}}\right) + e\left(\frac{H_w}{\sqrt{K}}\right) e\left(\frac{z}{\sqrt{K}}\right)}{\left[1 + e\left(\frac{H_w}{\sqrt{K}}\right)\right]} \right\} \quad \text{where } i = x, y \tag{10}$$

$$P_l = \frac{\mu_l}{Kh_{fg}\rho_l H_w} \left[\sum_{m=1}^{\infty} C_{m0} \cos(m\pi X) + \sum_{n=1}^{\infty} C_{0n} \cos(n\pi Y) + \sum_{n=1}^{\infty} \sum_{m=1}^{\infty} C_{mn} \cos(m\pi X) \cos(n\pi Y) \right] \left\{ 1 - \frac{1}{H_w} \frac{2\sqrt{K} \left(e\left(\frac{H_w}{\sqrt{K}}\right) - 1 \right)}{\left[1 + e\left(\frac{H_w}{\sqrt{K}}\right)\right]} \right\} \tag{15}$$

where H_w , K , P_l and μ are the wick height, the permeability, the liquid pressure and the viscosity of the working fluid, respectively. Integration of Eq. (10) with respect to the z-direction, yields the x- and y-averaged velocities through the mesh wick as:

$$\langle \vec{U}_x \rangle = -\frac{\partial P_l}{\partial x} \frac{K}{\mu} \left\{ 1 - \frac{1}{H_w} \frac{2\sqrt{K} \left(e\left(\frac{H_w}{\sqrt{K}}\right) - 1 \right)}{\left[1 + e\left(\frac{H_w}{\sqrt{K}}\right)\right]} \right\},$$

$$\langle \vec{U}_y \rangle = -\frac{\partial P_l}{\partial y} \frac{K}{\mu} \left\{ 1 - \frac{1}{H_w} \frac{2\sqrt{K} \left(e\left(\frac{H_w}{\sqrt{K}}\right) - 1 \right)}{\left[1 + e\left(\frac{H_w}{\sqrt{K}}\right)\right]} \right\} \tag{11}$$

where $\langle \vec{U}_x \rangle$ and $\langle \vec{U}_y \rangle$ are the averaged liquid velocities in x- and y-directions, respectively.

The continuity equation for the liquid flow is given by:

$$\frac{\partial \langle \vec{U}_x \rangle}{\partial x} + \frac{\partial \langle \vec{U}_y \rangle}{\partial y} = \frac{1}{h_{fg}\rho_l H_w} \varphi|_{z=0} \quad \text{where } \varphi|_{z=0} = \varphi_o \cdot Bi \cdot T^*|_{z=0} \tag{12}$$

Substitution of the x- and y-velocity components given in Eq. (11) into Eq. (12) and rearranging gives:

$$\frac{\partial^2 P_l}{\partial x^2} + \frac{\partial^2 P_l}{\partial y^2} = \frac{\mu_l}{Kh_{fg}\rho_l H_w} \left\{ 1 - \frac{1}{H_w} \frac{2\sqrt{K} \left(e\left(\frac{H_w}{\sqrt{K}}\right) - 1 \right)}{\left[1 + e\left(\frac{H_w}{\sqrt{K}}\right)\right]} \right\} \varphi_o \cdot Bi \cdot T^*|_{z=0} \tag{13}$$

where h_{fg} and ρ_l are the latent heat of vaporization and the liquid density, respectively. The pressure boundary conditions are given by:

$$\frac{\partial P_l}{\partial x} \Big|_{x=0} = \frac{\partial P_l}{\partial x} \Big|_{x=a} = \frac{\partial P_l}{\partial y} \Big|_{y=0} = \frac{\partial P_l}{\partial y} \Big|_{y=b} = 0 \tag{14}$$

Using the pressure boundary conditions given in Eq. (14), the modified liquid pressure distribution considering the no-slip condition at the wall of FMHPs becomes:

Substituting Eq. (7) and (15) into Eq. (13), the Fourier series coefficients of C_{m0} , C_{0n} , C_{mn} are obtained as:

$$C_{m0} = \varphi_o Bi \left(\frac{a}{m\pi}\right)^2 A_{m0}(0), \quad C_{0n} = \varphi_o Bi \left(\frac{b}{n\pi}\right)^2 A_{0n}(0),$$

$$C_{mn} = \varphi_o Bi \left(\frac{1}{\left(\frac{m\pi}{a}\right)^2 + \left(\frac{n\pi}{b}\right)^2}\right) A_{mn}(0) \tag{16}$$

where

$$A_{m0}(0) = \frac{2B_{m0}}{[m\pi C + Bi] \exp(m\pi C) - [m\pi C - Bi] \exp(-m\pi C)},$$

$$A_{0n}(0) = \frac{2B_{0n}}{B[(n\pi C + B - Bi) \exp\left(\frac{n\pi C}{B}\right) - (n\pi C - B - Bi) \exp\left(-\frac{n\pi C}{B}\right)]},$$

$$A_{mn}(0) = \frac{2B_{mn}}{(G\pi C + Bi) \exp(G\pi C) - (G\pi C - Bi) \exp(-G\pi C)}, \quad G = \sqrt{m^2 + \left(\frac{n}{b}\right)^2}.$$

where the Fourier coefficients, B_{m0} , B_{0n} , and B_{mn} , were described in Lefevre and Lallemand [5] and Rulliere et al. [6].

b. Vapor pressure distribution

In this paper, the vapor flow model presented by Lefevre and Lallemand [5] and Rulliere et al. [6] was used where the vapor pressure is given by:

$$P_v = -\frac{12\mu_v}{h_{fg}\rho_v (H_{total} - H_w)^3} \times \left[\sum_{m=1}^{\infty} C_{m0} \cos(m\pi X) + \sum_{n=1}^{\infty} C_{0n} \cos(n\pi Y) + \sum_{n=1}^{\infty} \sum_{m=1}^{\infty} C_{mn} \cos(m\pi X) \cos(n\pi Y) \right] \tag{17}$$

where the P_v , μ_v and H_{total} are the vapor pressure, the vapor viscosity, and the total summation of the wick and the vapor height,

respectively. The Fourier series coefficients of C_{m0} , C_{0n} , C_{mn} are the same as those given by Eq. (16).

2.3. Theoretical approach for maximum heat transfer rate of FMHPs

The Young-Laplace equation has been previously used to determine the maximum heat transfer rate of FMHPs using the capillary limit [5–8,10,26]. However, previous research did not consider whether the maximum surface temperature of FMHPs at the maximum heat transfer rate exceeded the allowable maximum temperature of the electronic components, which is crucial for ensuring the longevity of these components. In other words, an essential design criterion is that the calculated maximum heat transfer rate at the capillary limit should correspond to a temperature that is less than the allowable maximum temperature of the electronic component. Therefore, the maximum heat transfer rate of an FMHP is determined by using the Young-Laplace equation at the capillary limit with multi-heat sources and sinks as:

$$\Delta P_{capillary} = \Delta P_l + \Delta P_v \quad \text{where} \quad \Delta P_{capillary} = \frac{2\sigma}{r_{eff}} \cos \theta \quad (18)$$

where $\Delta P_{capillary}$, r_{eff} , σ and θ are the capillary pressure, the effective pore radius, the surface tension and the contact angle, respectively. The next step is to obtain the maximum surface temperature of a FMHP and the corresponding maximum heat transfer rate using Eqs. (6) and (7). If the maximum surface temperature is larger than the allowable maximum temperature limit, which is defined as the maximum temperature permitted for normal operation of electronic components, then the reported maximum heat transfer rate of FMHPs was reduced to match that which is associated with the maximum allowable temperature. Under this condition, the maximum heat transfer was recalculated as the heat transfer of the FMHP that occurred at the maximum allowable temperature. In this paper, we define the allowable maximum temperature limit to be 80 °C because the performance of electronic components in mobile devices can be dramatically decreased above 80 °C [27,28].

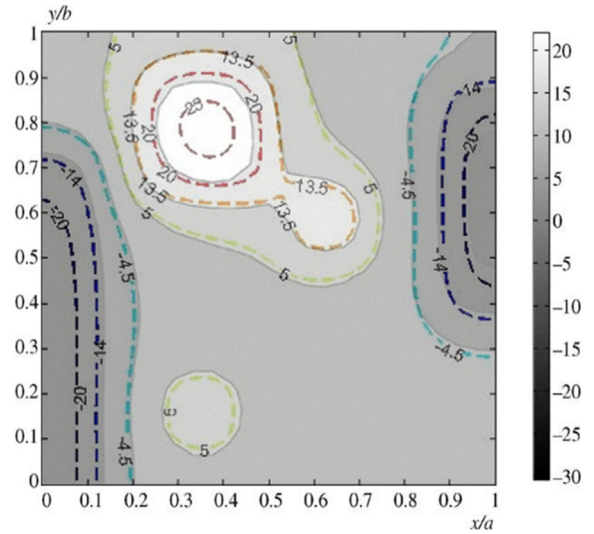
The effects of engineering parameters of the mesh-wick on the maximum theoretical heat transfer rate of an FMHP are presented. For a given material and working fluid, the key mesh wick characteristics, according to Eqs. (15), (17) and (18), that affect the maximum heat transfer are its permeability (K), its porosity (ε), and its height (H_w). These parameters can be simplified and interpreted as fiber diameter (d), fiber separation distance (w) and wick thickness (H_w) so that the permeability and the porosity of the mesh-screen wick [26] and the effective pore radius [26] are given by:

$$K = \frac{d^2 \varepsilon^3}{122(1 - \varepsilon)^2}, \quad \varepsilon = 1 - \frac{1.05\pi Nd}{4}, \quad N = \frac{1}{d + w}, \quad r_{eff} = \frac{d + w}{2} \quad (19)$$

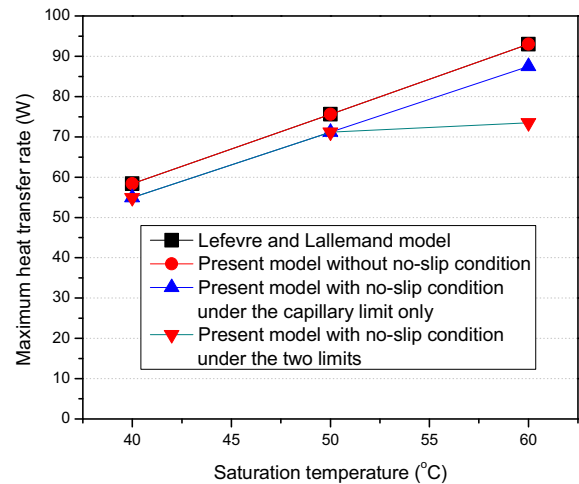
where ε and N are the porosity and the number of mesh layers in the wick, respectively. The mesh diameter and fiber separation distance are shown schematically in Fig. 2(b).

3. Validation

Fig. 3 illustrates the significance of neglecting the no-slip condition and the maximum allowable temperature limit on the calculation of the maximum heat transfer rate. For the analysis, the specifications for the heat pipes, including materials properties and other parameters, were chosen to be same with those of Lefevre and Lallemand [5], which are summarized in Table 1. The color, dotted lines shown in the Fig. 3(a) are temperature contour lines that were calculated with the present model and the gray shading are results from the Lefevre and Lallemand [5]. The present model with accounting for the only capillary limit instead of no-



(a) Validation for temperature (°C) distribution



(b) Validation for maximum heat transfer rate

Fig. 3. Validation results.

Table 1 Specifications of the FMHP (Flat-micro heat pipe).

Parameters	Specification
Heat pipe length (a)	40 mm
Heat pipe breadth (b)	40 mm
Heat pipe height (c)	900 μ m
Wall thickness (T_{wall})	265 μ m
Wick thickness (H_w)	140 μ m
Vapor space height (H_v)	230 μ m
Working fluid	Water
Mesh type	Copper
Diameter (d)	35 μ m
Fiber separation distance (w)	42 μ m
Position of heat source 1	8 mm $\leq x \leq 20.3$ mm 25.2 mm $\leq y \leq 37.2$ mm
Position of heat source 2	22 mm $\leq x \leq 28.8$ mm 20 mm $\leq y \leq 26.8$ mm
Position of heat source 3	11.2 mm $\leq x \leq 16$ mm 4 mm $\leq y \leq 8.8$ mm
Position of heat sink 1	0 mm $\leq x \leq 4.8$ mm 0 mm $\leq y \leq 30$ mm
Position of heat sink 2	35.2 mm $\leq x \leq 40$ mm 14 mm $\leq y \leq 36$ mm

slip condition and the two limits well matches the contours of Lefevre and Lallemand [5], while the value of most temperatures are within ± 1 °C. Fig. 3(b) compares the Lefevre and Lallemand

[5] model to the present analytical solution for three different cases. The first case with the red cycle symbol was used to validate the present model with the Lefevre and Lallemand [5] model by accounting for the only capillary limit without no-slip condition. For this case, the present model is in good agreement with the Lefevre and Lallemand [5] solution differing by less than 1%. However, as shown in Fig. 3(b), the maximum heat transfer rate of the FMHPs with no-slip condition and the capillary limit is as much as 6% lower than that of the results presented by Lefevre and Lallemand [5]. An even larger effect of improved modelling/design is observed when no-slip condition and the allowable electronic component maximum temperature limit under the capillary limit are both considered: the maximum heat transfer rate of the FMHPs is approximately 28% less than that for the Lefevre and Lallemand [5] model.

4. Results and discussion

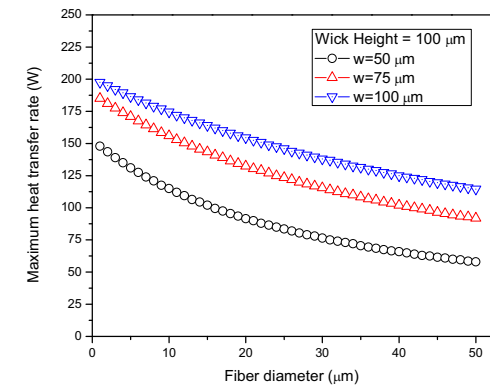
4.1. Effect of the fiber diameter (*d*) on the maximum heat transfer rate of FMHPs

Fig. 4 illustrates that consideration of the allowable temperature limit of electronic components together with the capillary limit leads to a maximum heat flux design that differs considerably from that when the capillary limit is considered alone. Fig. 4(a) and (b) shows the effect of the fiber diameter (*d*) on the maximum heat transfer rate for fixed fiber separation distance (*w*) and wick thickness ($H_w = 100 \mu\text{m}$). Fig. 4(a) shows that, when the maximum heat transfer rate is analytically obtained while only considering the capillary limit, the maximum heat transfer rate decreases as the fiber diameter increases for fixed parameters.

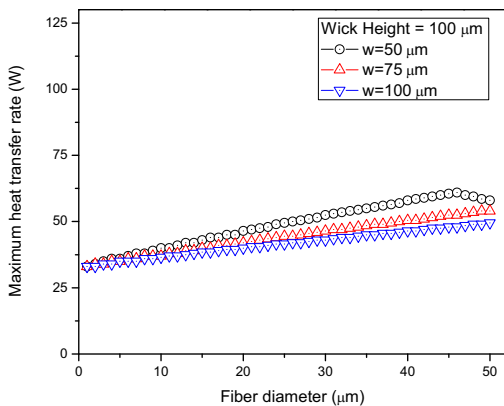
As the fiber diameter increases, the driving force of the capillary pressure is reduced according to Eq. (18) due to the increase in r_{eff} . In addition, because *w* is fixed, an increase in the fiber diameter increases the liquid pressure drop. As a result, the liquid mass flow through the fibers of the wick is reduced and the maximum heat flux of the FMHP correspondingly decreases with increasing fiber diameter. In contrast, as shown in Fig. 4(b), the inclusion of the maximum allowable temperature limit causes increasing fiber diameter to have the opposite effect on the maximum heat transfer rate of the FMHP. Fig. 4(b) shows that the maximum heat transfer rate of the FMHP increases with the fiber diameter except for $w = 50 \mu\text{m}$ and fiber diameters larger than $45 \mu\text{m}$. Under these conditions, this is primarily because the effective thermal conductivity of the wick structure increases for fixed conditions as the fiber diameter increases. However, at $w = 50 \mu\text{m}$ and fiber diameters larger than $45 \mu\text{m}$, the capillary limit dominates, and the maximum heat flux decreases while the fiber diameter increases from $45 \mu\text{m}$ to $50 \mu\text{m}$. Moreover, for the most of the examined constraints, Fig. 4(b) shows that consideration of the maximum allowable temperature limit ($80 \text{ }^\circ\text{C}$) is crucial for the design of FMHPs because, for this condition, the maximum heat transfer rate is less than half of that when only the capillary limit is considered.

4.2. Effect of the fiber separation distance (*w*) on the maximum heat transfer rate of FMHPs

Fig. 5 shows the effect of the fiber separation distance (*w*) on the maximum heat transfer rate for a fixed H_w of $100 \mu\text{m}$ and three

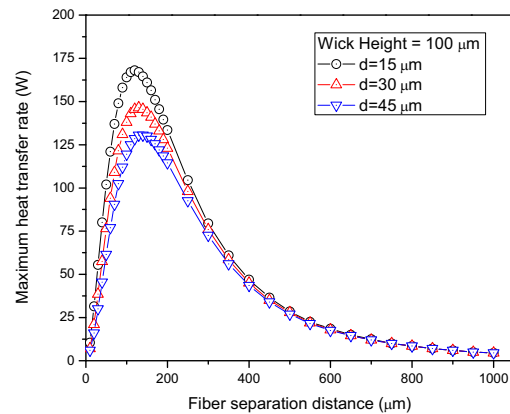


(a) Capillary limit

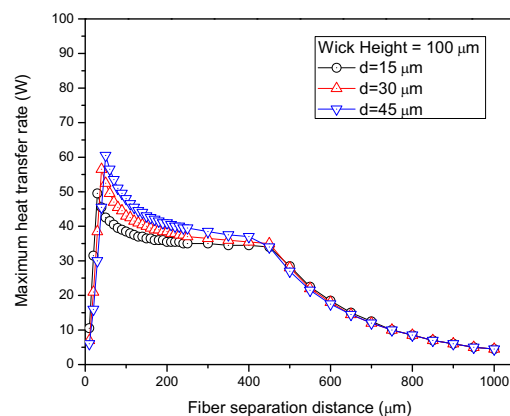


(b) Capillary limit and allowable maximum temperature limit ($80 \text{ }^\circ\text{C}$)

Fig. 4. Effect of fiber diameter on the maximum heat transfer rate of FMHPs.



(a) Capillary limit



(b) Capillary limit and allowable maximum temperature limit ($80 \text{ }^\circ\text{C}$)

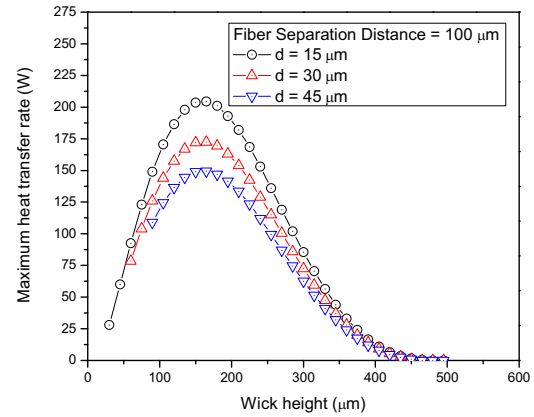
Fig. 5. Effect of fiber separation distance on the maximum heat transfer rate of FMHPs.

different fixed fiber diameters (d). The maximum heat transfer rate calculated by considering only the capillary limit is shown in Fig. 5 (a). Fig. 5(a) exhibits an optimum fiber separation distance (w) due to the competing effects of increasing the fiber separation distance on the mass flow rate through the wick. The first effect is the increment of the mass flow rate because the liquid pressure drop is decreased. The second effect is the decrement of the mass flow rate because the capillary limit is decreased. However, as shown in Fig. 5(b), the maximum heat transfer rate of the FMHPs calculated by considering the two limits according to the fiber separation distance shows different behaviors compared with the results at the capillary limit only. For example, at the range of the fiber separation distance from $40\ \mu\text{m}$ to $450\ \mu\text{m}$ and the fiber diameter of $15\ \mu\text{m}$, the maximum surface temperature at the maximum heat transfer rate calculated at the capillary limit is larger than the allowable maximum temperature limit. The maximum heat transfer rate of the region was recalculated to satisfy the allowable maximum temperature. As a result, the maximum heat transfer rate in the region is decreased with the increment of the fiber separation distance because the effective thermal conductivity of wick structure occupied by working fluids is decreased as the fiber separation distance increases. Moreover, comparison of Fig. 5 (a) and (b) illustrates the importance of considering both the capillary limit and the allowable maximum temperature limit on calculating the maximum heat transfer rate of the FMHPs. The comparison shows that consideration of both limits results in roughly a 70% smaller optimal heat transfer rate that occurs at a smaller w ($50\ \mu\text{m}$ rather than $150\ \mu\text{m}$) than when only the capillary limit is considered. For fiber separation distances larger than $450\ \mu\text{m}$, the calculated maximum heat transfer rates are essentially the same for the two limits.

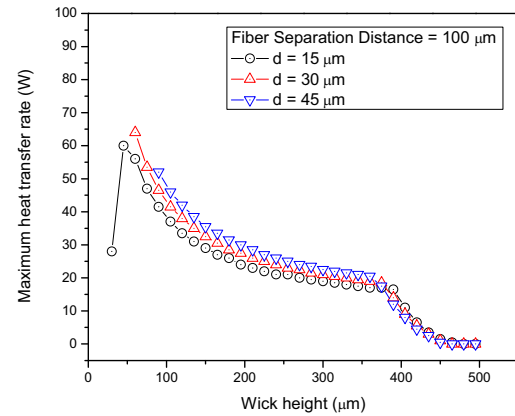
4.3. Effect of the wick thickness (H_w) on the maximum heat transfer rate of FMHPs

Fig. 6 shows the effect of the wick thickness (H_w) on the maximum heat transfer rate for a fiber separation distance of $100\ \mu\text{m}$ and three different fixed fiber diameters ($15\ \mu\text{m}$, $30\ \mu\text{m}$, and $45\ \mu\text{m}$). As shown in Fig. 6(a), with consideration of only the capillary limit, an optimum maximum heat transfer rate exists for a particular wick thickness (H_w), which is due to the balance between increasing vapor pressure and decreasing liquid pressure with increasing wick thickness, with all other parameters fixed. As a result, the total pressure increases and then decreases with respect to increasing wick thickness and the maximum heat transfer rate follows the total pressure.

However, as shown in Fig. 6(b), similar behavior of the fiber separation distance's effect on the maximum heat transfer is observed at both capillary limit and allowable maximum temperature limit. For example, at the wick height range from $60\ \mu\text{m}$ to $375\ \mu\text{m}$ and the fiber diameter of $15\ \mu\text{m}$, the maximum surface temperature at the maximum heat transfer rate calculated at the capillary limit is larger than the allowable maximum temperature limit. So, the maximum heat transfer rate of FMHPs which can be satisfied by the allowable maximum temperature limit was recalculated as shown in Fig. 6(b). Also, in the region the maximum heat transfer rate is decreased with the increment of the wick height because the thermal resistance of wick structure filled with working fluids is increased with the wick height. Comparison of Fig. 6(a) and (b) illustrates the effect of considering both limits on the analysis. Inclusion of both the capillary limit and the allowable temperature limit affects the results for wick thicknesses less than approximately $375\ \mu\text{m}$. For example, for wick thickness between $60\ \mu\text{m}$ and $375\ \mu\text{m}$, the maximum heat transfer rate using both limits is roughly 70% less than that for just the capillary limit.



(a) Capillary limit



(b) Capillary limit and allowable maximum temperature limit ($80\ ^\circ\text{C}$)

Fig. 6. Effect of wick thickness on the maximum heat transfer rate of FMHPs.

4.4. Maximum heat transfer rate of FMHPs with optimized wick geometry

The present model was used to optimize the wick geometry and to demonstrate that the maximum heat transfer can be severely overestimated if the allowable maximum temperature limit is not considered. Table 1 shows typical geometry and material specifications for a FMHP. The analysis was done for two mesh wick layers ($N = 2$), which leads to a wick thickness of:

$$H_w = 2Nd \tag{20}$$

where N is the number of the mesh wick's layer. Fig. 7 shows the contour map of maximum heat transfer rate for a FMHP with two layers of a mesh wick as a function of the fiber diameter and the fiber separation distance. Fig. 7(a) shows the analysis for only the capillary limit, which gives an optimized fiber diameter of $34\ \mu\text{m}$ and a fiber separation distance of $100\ \mu\text{m}$ of the FMHP with maximum heat transfer rate of $161\ \text{W}$. Compare this to Fig. 7(b), which shows the analysis accounting for both limits, where the optimized geometry of the FMHP for a fiber diameter of $12\ \mu\text{m}$ and a fiber separation distance of $100\ \mu\text{m}$ gave a maximum heat transfer rate of $65\ \text{W}$ at the maximum allowable component temperature limit of $80\ ^\circ\text{C}$. The comparison clearly shows that for the optimized wick geometry, the maximum heat transfer rate is overestimated when the allowable maximum temperature of electronic components is not considered. Moreover, Fig. 8 shows the surface temperature

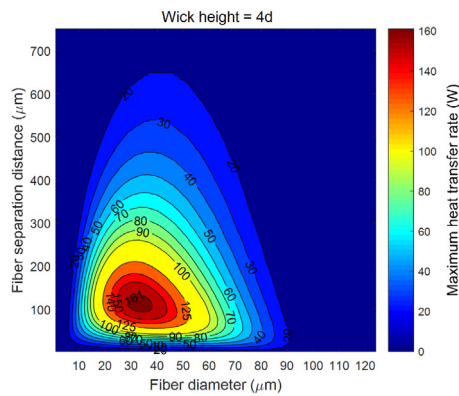
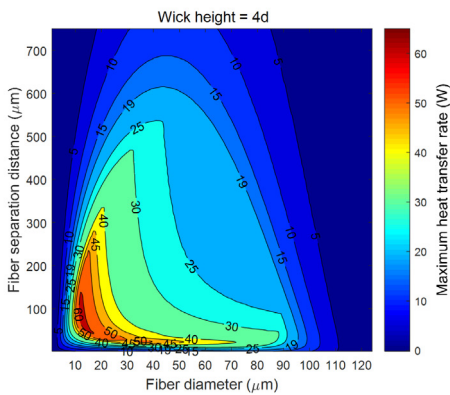
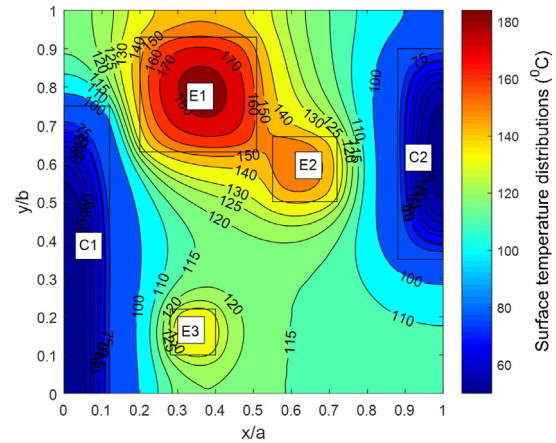
(a) Capillary limit ($w = 100 \mu\text{m}$)(b) Capillary limit and allowable maximum temperature limit (80 °C) with $w = 100 \mu\text{m}$

Fig. 7. Optimization results of FMHP with mesh wick of two layer.

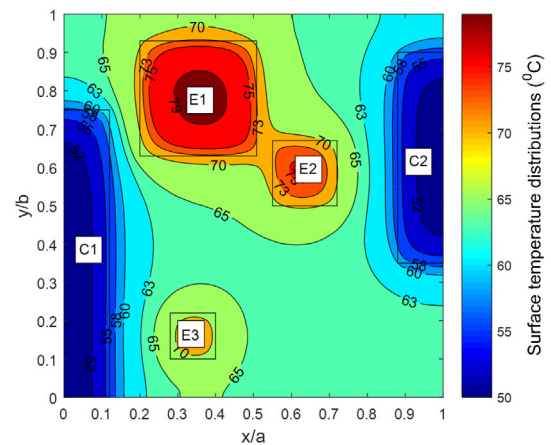
distributions of the FMHP with the optimized mesh wick under the capillary limit only and the two limits, respectively. Fig. 8(a) shows the maximum surface temperature of the FMHP is 180 °C with the maximum heat transfer rate of 161 W. A FMHP cannot operate at the maximum heat transfer rate because the electronic components would fail at a temperature greater than 80 °C. By comparison, Fig. 8 (b) shows the temperature distribution with the maximum surface temperature of 80 °C with the maximum heat transfer rate of 65 W; this is at the allowable maximum temperature of electronic components. Finally, the maximum heat transfer rate for the optimized mesh wick geometry with the number of mesh wick's layers from 1 to 6 is shown in Table 2.

5. Conclusion

This paper presents an investigation, including an analytical model, of the effect of the mesh wick geometry on the maximum heat transfer rate of the FMHPs with multi-heat sources and sinks. The analysis considers the no-slip condition using the Brinkman-extended Darcy equation, the pressure distribution, and the temperature distribution of FMHPs with multi-heat sources and sinks. The mesh wick fiber diameter, fiber separation distance, and wick thickness are identified with the model as key parameters that govern the maximum heat transfer rate of the FMHPs. The effect of these key parameters on the maximum heat transfer rate of the FMHP is analytically investigated for two special cases or two limits. One is the capillary limit and the other limit is the allowable maximum temperature limit. The latter limit is used to ensure that the surface temperature of the FMHP with the maximum heat transfer rate calculated at the capillary limit does not exceed the



(a) Capillary limit only



(b) Capillary limit and allowable maximum temperature limit (80 °C)

Fig. 8. Surface temperature distributions of the FMHPs with optimized mesh wick of two layers.

Table 2

Optimized wick geometries for the FMHP with maximum heat transfer rate.

Mesh Wick's Layer	Both limits (Capillary Limit and Allowable Maximum Temperature Limit)			
	d (μm)	w (μm)	H_w (μm)	Q_{max} (W)
1	26	110	54	68.0
2	12	100	48	65
3	8	70	48	64.0
4	6	70	48	62.5
5	5	60	50	61.0
6	4	60	48	60.5

allowable maximum temperature of the electronic components. The maximum heat transfer rate of the FMHPs for the two limits is shown to differ significantly depending on the variation of key geometric parameters. A comparison of the maximum heat transfer rate and the surface temperature distribution of the FMHP with the optimized wick under the capillary limit only and under both limits is presented.

Conflict of interest

The authors declared that there is no conflict of interest.

Acknowledgment

This work was supported by a grant from the Space Core Technology Development Program of National Research Foundation of Korea (NRF) funded by the Korean Government (MSIP) (NRF-2015M1A3A3A02014936).

References

- [1] S.S. Hsieh, R.Y. Lee, J.C. Shyu, S.W. Chen, Thermal performance of flat vapor chamber heat spreader, *Energy Convers. Manage.* 49 (2008) 1774–1784.
- [2] S.S. Hsieh, R.Y. Lee, Design, fabrication and performance tests for a polymer-based flexible flat heat pipe, *Energy Convers. Manage.* 70 (2013) 10–19.
- [3] B. Salami, H. Noori, F. Mehdipour, M. Baharani, Physical-aware predictive dynamic thermal management of multi-core processors, *J. Parallel Distrib. Comput.* 95 (2016) 42–56.
- [4] T.Q. Feng, J.L. Xu, An analytical solution of thermal resistance of cubic heat spreaders for electronic cooling, *Appl. Therm. Eng.* 24 (2004) 323–337.
- [5] F. Lefevre, M. Lallemand, Coupled thermal and hydrodynamic models of flat micro heat pipes for the cooling of multiple electronic components, *Int. J. Heat Mass Transf.* 49 (2006) 1375–1383.
- [6] R. Rulliere, F. Lefevre, M. Lallemand, Prediction of the maximum heat transfer capability of two-phase heat spreaders – experimental validation, *Int. J. Heat Mass Transf.* 50 (2007) 1255–1262.
- [7] S. Lips, F.M. Lefevre, A general analytical model for the design of conventional heat pipes, *Int. J. Heat Mass Transf.* 72 (2014) 288–298.
- [8] K.Y. Do, S.J. Kim, S.V. Garimella, A mathematical model for analyzing the thermal characteristics of a flat micro heat pipe with a grooved wick, *Int. J. Heat Mass Transf.* 51 (2008) 4637–4650.
- [9] R. Revellin, R. Rulliere, F. Lefevre, J. Bonjour, Experimental validation of an analytical model for predicting the thermal and hydrodynamic capabilities of flat micro heat pipes, *Appl. Therm. Eng.* 29 (2009) 1114–1122.
- [10] K.H. Do, S.P. Jang, Effect of nanofluids on the thermal performance of a flat micro heat pipe with a rectangular grooved wick, *Int. J. Heat Mass Transf.* 53 (2010) 2183–2192.
- [11] H. Peng, J. Li, X. Ling, Study on heat transfer performance of an aluminum flat plate heat pipe with fins in vapor chamber, *Energy Convers. Manage.* 74 (2013) 44–50.
- [12] J.P. Longtin, B. Badran, F.M. Gerner, A one-dimensional model of a micro heat pipe during steady-state operation, *J. Heat Transf.* 116 (1994) 709–715.
- [13] D.A. Benson, R.T. Mitchell, M.R. Tuck, D.W. Palmer, G.P. Peterson, Ultrahigh-capacity micromachined heat spreaders, *Microscale Thermophys. Eng.* 2 (1998) 21–30.
- [14] V. Sartre, M.C. Zaghoudi, M. Lallemand, Effect of interfacial phenomena on evaporative heat transfer in micro heat pipes, *Int. J. Therm. Sci.* 39 (2000) 498–504.
- [15] Y.X. Wang, H.B. Ma, G.P. Peterson, Investigation of the temperature distribution on radiator fins with micro heat pipes, *J. Thermophys. Heat Transf.* 15 (2001) 42–49.
- [16] Y.X. Wang, G.P. Peterson, Analysis of wire-bonded micro heat pipe arrays, *J. Thermophys. Heat Transf.* 16 (2002) 346–355.
- [17] M.L. Berre, S. Launay, V. Sartre, M. Lallemand, Fabrication and experimental investigation of silicon micro heat pipes for cooling electronics, *J. Micromech. Microeng.* 13 (2003) 436–441.
- [18] S. Khandekar, M. Groll, V.V. Luckchoura, W. Findl, J. Zhuang, Micro heat pipes for stacked 3D microelectronic modules, in: *ASME 2003 International Electronic Packaging Technical Conference and Exhibition*, 2003, pp. 245–251.
- [19] S. Launay, V. Sartre, M.B.H. Mantelli, K.V. de Paiva, M. Lallemand, Investigation of a wire plate micro heat pipe array, *Int. J. Therm. Sci.* 43 (2004) 499–507.
- [20] X.Y. Huang, C.Y. Liu, The pressure and velocity fields in the wick structure of a localized heated flat plate heat pipe, *Int. J. Heat Mass Transf.* 39 (1996) 1325–1330.
- [21] W. Qin, C.Y. Liu, Liquid flow in the anisotropic wick structure of a flat plate heat pipe under block-heating condition, *Appl. Therm. Eng.* 17 (1997) 339–349.
- [22] B.K. Tan, X.Y. Huang, T.N. Wong, K.T. Ooi, A study of multiple heat sources on a flat plate heat pipe using a point source approach, *Int. J. Heat Mass Transf.* 43 (2000) 3755–3764.
- [23] M. Kaviany, *Principles of Heat Transfer in Porous Media*, Springer Science & Business Media, 2012.
- [24] M. Kaviany, Non-Darcian effects on natural convection in porous media confined between horizontal cylinders, *Int. J. Heat Mass Transf.* 29 (1986) 1513–1519.
- [25] S.B. Kim, K.H. Kim, M.A. Kedzierski, S.P. Jang, Thermal characteristics of silicon wafer-based TVCs (thin vapor chambers) with disk-shaped using DI water, *Int. J. Heat Mass Transf.* 127 (2018) 526–534.
- [26] A. Faghri, *Heat Pipe Science and Technology*, Taylor and Francis, 1994.
- [27] M.K. Berhe, Ergonomic temperature limits for handheld electronic devices, in: *ASME 2007 InterPACK Conference collocated with the ASME/JSME 2007 Thermal Engineering Heat Transfer Summer Conference*, 2007, pp. 1041–1047.
- [28] G.R. Wagner, W. Maltz, On the thermal management challenges in next generation handheld devices, *ASME 2013 International Technical Conference and Exhibition on Packaging and Integration of Electronic and Photonic Microsystems*, 2013, pp. V002T08A046–V002T08A046.